Available online at www.sciencedirect.com
SCIENCE DIRECT®
International Journal of Heat and Mass Transfer 48 (2005) 3574–3590
International Journal of HEAT and MASS TRANSFER
www.elsevier.com/locate/ijhmt

Effect of a swirling ladle shroud on fluid flow and mass transfer in a water model of a tundish

G. Solorio-Díaz [a], R.D. Morales [a,b,*], A. Ramos-Banderas [a]

[a] Department of Metallurgy and Materials Engineering, National Polytechnic Institute-ESIQIE, Apdo. Postal 75874, Mexico D.F., C.P. 07338, Mexico
[b] K&E Technologies S.A. de C.V., And. 8 de Fdo. Amilpa No. 7, Col. CTM-Risco, Mexico D.F., CP 07090, Mexico

Received 18 April 2004; received in revised form 4 March 2005
Available online 11 May 2005

Abstract

A swirling ladle shroud (SLS) is used to control flow turbulence and to improve flotation of inclusions in a two-strand tundish of a slab caster. To simulate the fluid flow in a swirling flow three turbulence models, k–ε, k–ω and RSM were employed. Using the mixing kinetics of a tracer as well as Particle Image Velocimetry (PIV) determinations it was found that among these three models the model of turbulence RSM predicts with acceptable agreement the velocity fields of swirling flows experimentally measured. The SLS decreases the turbulence of the entering jet and of the complete flow field when it is compared with a conventional ladle shroud. Kinetic energy of fluid is dissipated through recirculating flows in the transversal and horizontal planes of the tundish helping to the flotation of inclusions through buoyancy, drag and inertial forces. The SLS will become in a new generation of flow control devices in continuous casters of steel.

Keywords: Swirling flow; Tundish; Turbulence models; Flow control; Mass transfer; Velocity field; PIV; Reynolds stresses

1. Introduction

Control of liquid steel turbulence in tundishes is of a paramount importance in order to avoid flux entrapment and pickup of oxygen and nitrogen from the surrounding atmosphere, to decrease or eliminate the existence dead zones and to perform efficient mechanisms for floating inclusions. To accomplish these functions various flow control devices (FCD) have been designed including weirs, dams, baffles, etc., Heaslip et al. [1]. Recently turbulence inhibitors have shown excellent performances as FCD's to attain all the objectives mentioned here. The authors have studied the effects of turbulence inhibitors on flotation rate of inclusions, López-Ramirez et al. [2] and thermal stratification of flows Vargas-Zamora et al. [3], López-Ramírez et al. [4] and Morales et al. [5,6].

Another approach for fluid flow control in tundishes consists of using a combination of gas bubbling and a turbulence inhibitor as has been reported by Ramos-Banderas et al. [7] who employed mathematical simulations,

* Corresponding author. Address: Department of Metallurgy and Materials Engineering, National Polytechnic Institute-ESIQIE, Apdo. Postal 75874, Mexico D.F., C.P. 07338, Mexico. Tel./fax: +52 55 57296000.
E-mail addresses: rmorales@ipn.mx, ketechnologies@prodigy.net.mx (R.D. Morales).

0017-9310/$ - see front matter © 2005 Elsevier Ltd. All rights reserved.
doi:10.1016/j.ijheatmasstransfer.2005.03.007

Nomenclature

D_{nozzle}	bore size of ladle shroud
f_β	a pseudo-constant, which is a function of another one named X_ω in the k–ω model, see Table 2
f_β^*	a pseudo-constant, which is a function of X_k in the k–ω model, see Table 2
k	turbulent kinetic energy
l	eddy length
P	pressure
Q	flow rate of liquid
u_i	time averaged fluid velocity in direction "i"
u_j	time averaged fluid velocity in direction "j"
u_i'	turbulent fluctuation of fluid velocity in direction "i"
u_j'	turbulent fluctuation of fluid velocity in direction "j"
g	gravity constant
D_{eff}	effective mass transfer diffusivity
D_0	molecular diffusitivity of a tracer
M	total mass of the tracer
V	volume of the water column in the ladle shroud
F_{D}	drag coefficient
C	dimensionless concentration
Greek symbols	
α	a constant in the k–ω model equal to 13/25
β	a pseudo-constant given in Table 2
β_0	a constant in the k–ω model equal to 9/125
β^*	a pseudo-constant in the k–ω as function of β_0^* and the pseudo-constant f_β^* in the k–ω model
δ_{ij}	delta of Krocneker
X_ω	a pseudo-constant in the k–ω model
X_k	gradient of specific dissipation rate as a function of the scalar gradient of the kinetic turbulence energy in the k–ω model, see Table 2
ε	dissipation rate of kinetic energy
Ω_k	angular velocity
ω	specific dissipation rate of turbulent energy
ρ	density of fluid
σ	a constant equal to 1/2 in the k–ω model
σ^*	a constant equal to 1/2 in the k–ω model
σ_k	a constant in the k–ε model in the turbulent kinetic energy equation, see Table 1
σ_ε	a constant in the dissipation rate of the kinetic turbulent energy in the k–ε model, see Table 1
μ	fluid viscosity
μ_{eff}	effective viscosity of fluid
ν	is equal to μ/ρ, dynamic viscosity of fluid
ζ	random number in the random walk mode
θ	dimensionless time

Particle Image Velocimetry (PIV) measurements and tracer experiments in their study. They found that gas bubbling can be helpful to improve flotation of inclusions to some extent; when the flow rate of gas is excessive inclusions initiate a recirculation motion in the outlet box to get out finally toward the mold. These authors demonstrated that with an appropriate amount of gas combined with the use of turbulence inhibitor, it was possible to control flow turbulence and to improve the flotation rate of inclusions.

We propose a further simplification for fluid flow control consisting of a special design of the ladle shroud (LS), which would avoid the use of any furniture inside the tundish. That is, flow control should be performed from the entry jet rather than inside of the tundish. This approach would reduce the tundish preparation tasks at the casting floor as well as the costs of this operation. The concept consists of reducing the turbulent kinetic energy of the entry jet through a swirling fluid motion that will dissipate the turbulent energy before its impact on the tundish bottom. This is different to the concept of a turbulence inhibitor where fluid flow turbulence is controlled once the entry jet impacts the bottom. Fig. 1a and b show the designs of a conventional LS and the proposed swirling ladle shroud (SLS) at a scale of 1/3. The first one is a pipe with a slight inverted cone and the SLS consists of three chambers along a straight pipe, a blade in the upper part and a tip with a bell shape.

In the present work, various aspects of flow and mass transfer are studied through an isothermal water model, mathematical simulations, PIV measurements and tracer experiments. Firstly three turbulence models are tested in order to evaluate which of them is able to predict more closely the PIV determinations of fluid flow. Once a turbulence model is chosen the next step is the analysis of momentum and mass transfer using the SLS comparing the results with the conventional LS in a slab tundish. The final aim is to provide a complete overview of the feasibility of the SLS as a FCD that would substitute all other devices designed, up to now, for the same purposes. If the effects of a SLS using a blade to promote a swirling flow are positive, in the sense of a better flow control and to enhance the flotation rate of inclusions, the next development step is the substitution of the blade by another more practical device.

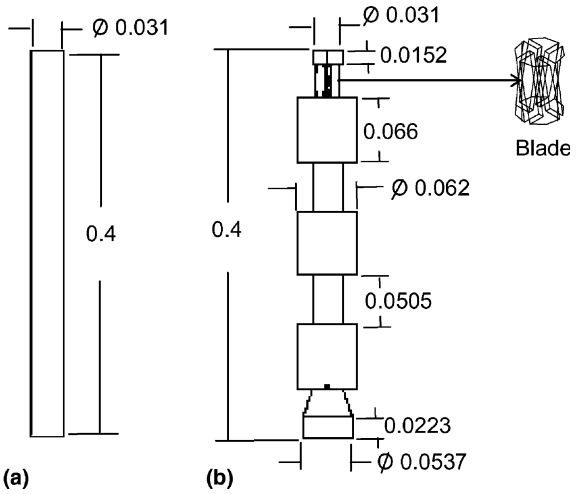

Fig. 1. Geometric dimensions of the experimental shrouds (m): (a) conventional ladle shroud (LS) and (b) swirling ladle shroud (SLS).

2. Experimentation

A 1/3 scale model that meets the Froude criterion was built. Neglecting the Reynolds criterion will change the magnitudes of the flow variables, mainly velocity fields in the model (velocities will be smaller), regarding the actual tundish. However, keeping the same Froude number will allow obtaining similar fluid flow patterns between both systems. Geometric dimensions of the model are shown in Fig. 2a and b. This model corresponds to the current tundish of the Company SIDOR in Venezuela of a two-strand slab caster. Mass transfer was modeled by means of a pulse injection of 20 cm^3 of red dye solution taken from a 35 g/l original solution. Tracer injection was performed in the LS during 3 s and the response of this signal, for tracer concentrations, was continuously monitored in one of the tundish outlets by pumping samples of liquid into a cell of a spectrophotometer. The readings of the tracer concentrations were recorded in a PC equipped with an acquisition card in real time. RTD curves were derived from the mixing kinetics of the tracer as explained by Vargas-Zamora et al. [3] (see Appendix A). These experiments were carried out under isothermal room temperature conditions. The conventional LS and the proposed SLS, Fig. 1a and b respectively were tested in these experiments. The flow rate of water into the LS or SLS was 5.7×10^{-4} m^3/s (34.2 l/min) equivalent to 90.47×10^{-4} m^3/s (3.8 ton/min) of liquid steel, according to the Froude criterion. This flow, once converted into flow rate of water yields a velocity of 0.77 m/s through the ladle shroud assuming a flat velocity profile.

Fluid flow structure was also monitored using a Particle Image Velocimetry (PIV) equipment from Dantec Systems. A green frequency double-pulsed Nd:YAG laser with a wavelength of 532 nm was employed for this purpose. Description of this technique has been explained somewhere else [3]. Fig. 3 shows a scheme of the experimental setup including the PIV equipment and the spectrophotometer to determine RTD curves form signals of the tracer.

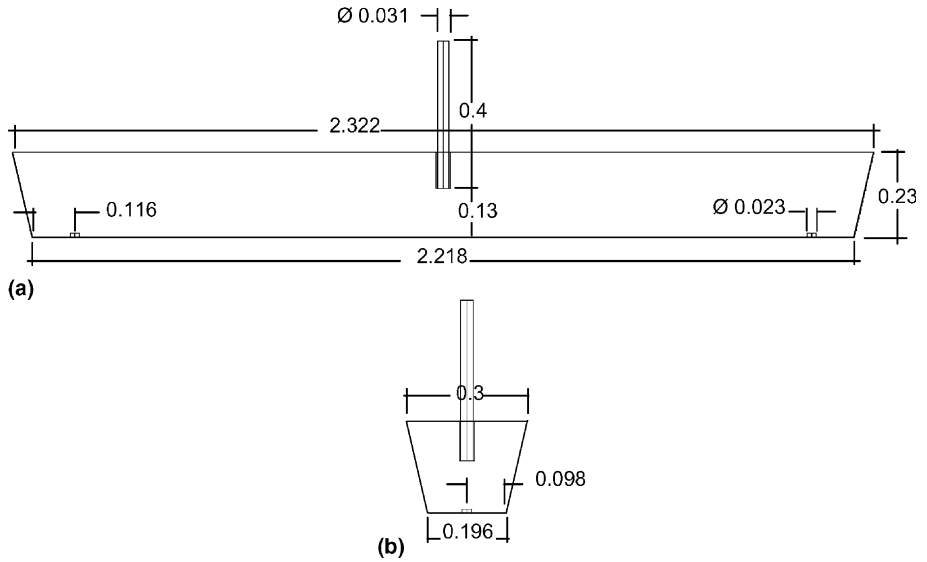

Fig. 2. The geometric dimensions of the tundish (m).

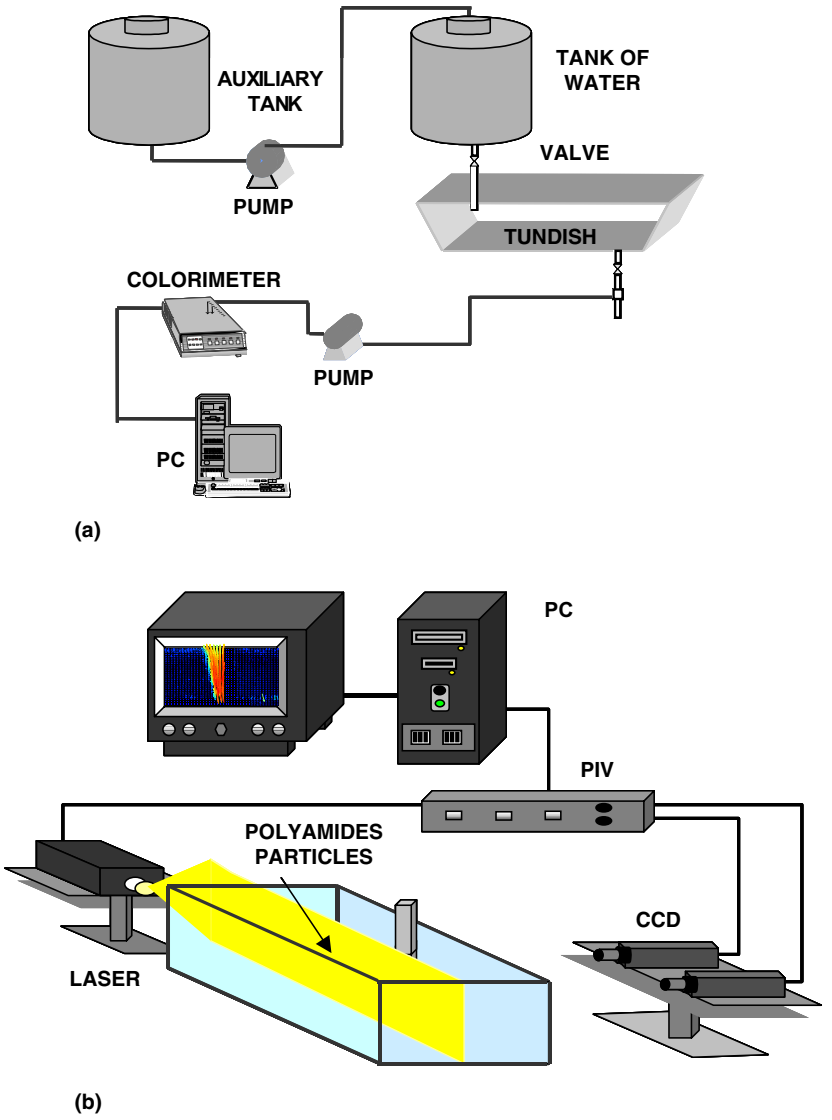

Fig. 3. (a) Schemes of the experimental arrangement including the particle image velocimetry and (b) tracer concentration detection system to determine RTD curves.

3. Mathematical models

The most commonly used turbulence model is that devised by Jones and Launder [8] and known as k–ε, it has many advantages; its concept is simple, is implemented in many commercial codes and it has demonstrated capability to simulate correctly many industrial processes like combustion, Lockwood and Romo-Millanes [9], fluid flow in tundishes Morales et al. [10] and multiphase flows in tundishes, Ramos-Banderas et al. [7] among many other applications. Nevertheless, it fails to provide reliable results of swirling flows and highly strained angular velocities of rotating flows, Launder and Shina [11]. Since we are dealing here with a complex swirling flow, two other turbulence models were tested against experimental results; the k–ω model of Wilcox [12] and the Reynolds Stress model (RSM) which uses additional equations to calculate the Reynolds stresses of the flow, Launder [13]. Here we summarize the main characteristics of each turbulence model.

3.1. k–ε model

The k–ε model, the k–ω model and the RSM models belong to a group of turbulence models known as Reynolds Average Navier–Stokes (RANS) that provides time-averaged flow variables. These variables can be dependent on time for cases of unsteady state flows.

The k–ε and k–ω models use the hypothesis of the isotropic eddy-viscosity, which is modeled through the flow fields of the turbulent kinetic energy and the specific dissipation rate. All simulations in this work are performed under steady state conditions, accordingly the transport equations of the k–ε model for an incompressible fluid are;

Equation of continuity

$$\frac{\partial}{\partial x_j}(u_j) = 0 \tag{1}$$

Momentum equation

$$\frac{\partial}{\partial x_j}(\rho u_i u_j) = -\frac{\partial P}{\partial x_i} + \frac{\partial}{\partial x_j}\left[\mu_{\text{eff}}\left(\frac{\partial u_i}{\partial u_j} + \frac{\partial u_j}{\partial x_i}\right)\right] - \frac{\partial(\overline{u_i' u_j'})}{\partial x_j} + \rho g \tag{2}$$

the closure of this system of partial differential equations is obtained through the equations shown in Table 1 which includes the transport equations for the turbulent kinetic energy, k, its dissipation rate, ε, the turbulent viscosity, $\mu_T(\mu_{\text{eff}} = \mu + \mu_T)$ and empirical constants.

3.2. k–ω model

This is an empirical model based also on modeling transport equations for the turbulence kinetic energy k and the specific dissipation rate ω, which can also be thought as the ratio of ε to k. Naturally continuity and momentum transfer are expressed also by Eqs. (1) and (2) and the closure for the system of equations is provided by equations of transport for the turbulent kinetic energy, k, and its specific dissipation rate, ω. The turbulent viscosity model and the empirical equations presented in Table 2 close the system of equations.

3.3. Reynolds stress model (RSM)

This model abandons the isotropic eddy-viscosity hypothesis and closes the RANS equations by solving transport equations for the Reynolds stresses, together with an equation for the dissipation rate. The transport equations for the Reynolds stresses can be expressed as,

$$\begin{aligned}
&\underset{C_{ij}}{\frac{\partial}{\partial x_k}(\rho u_k \overline{u_i' u_j'})} \\
&\quad = \underset{D_{T,ij}}{-\frac{\partial}{\partial x_k}\left[\overline{p(\delta_{kj} u_i' + \delta_{ik} u_j')}\right]} \\
&\qquad + \underset{D_{L,ij}}{\frac{\partial}{\partial x_k}\left[\mu \frac{\partial}{\partial x_k}(\overline{u_i' u_j'})\right]} - \underset{P_{ij}}{\rho\left(\overline{u_i' u_j'}\frac{\partial u_j}{\partial x_k} + \overline{u_j' u_k'}\frac{\partial u_i}{\partial x_k}\right)} \\
&\qquad + \underset{\Phi_{ij}}{\overline{p\left(\frac{\partial u_i'}{\partial x_j} + \frac{\partial u_j'}{\partial x_i}\right)}} \underset{\varepsilon_{ij}}{-2\mu\overline{\frac{\partial u_i}{\partial' x_k}\frac{\partial u_j'}{\partial x_k}}} \\
&\qquad \underset{F_{ij}}{-2\rho\Omega_k(\overline{u_j' u_m'}\varepsilon_{ikm} + \overline{u_i' u_m'}\varepsilon_{jkm})}.
\end{aligned} \tag{3}$$

where C_{ij} is convection term, $D_{T,ij}$ is turbulent diffusion, $D_{L,ij}$ is molecular diffusion, P_{ij} is stress production, Φ_{ij} is pressure strain, ε_{ij} is dissipation and F_{ij} is production term by system rotation. The turbulent diffusion, pressure strain and dissipation terms need to be modeled. Then $D_{T,ij}$ is evaluated using the gradient diffusion model of Daly and Harlow [14]. The pressure-strain term, Φ_{ij}, is modeled according to the proposals of Gibson and Launder [15] and Launder [16]. The dissipation term, ε_{ij}, is evaluated through the Sarkar model [17] as,

$$\varepsilon_{ij} = \frac{2}{3}\delta_j^i \rho\varepsilon \tag{4}$$

The turbulent kinetic energy for modeling a specific term is obtained through the trace of the Reynolds stress tensor:

$$k = \frac{1}{2}\overline{(u_i' u_j')} \tag{5}$$

$$k = \frac{1}{2}\overline{u_i' u_i'} \tag{6}$$

The scalar dissipation rate of the kinetic energy, ε, is calculated through an equation similar to that for the k–ε model given in Table 1. Similarly, the turbulent viscosity is also calculated through an equation that is similar to that for the k–ε model and is also given in Table 1.

3.4. Mass transfer

Unsteady state mass transfer affected by the fluid flow was simulated solving the following equation;

Table 1
The k–ε model of turbulence

Kinematic eddy viscosity	$\nu_T = C\mu k^2/\varepsilon$
Turbulence kinetic energy	$\frac{\partial k}{\partial t} + u_j\frac{\partial k}{\partial x_j} = \tau_{ij}\frac{\partial \ddot{u}_i}{\partial x_j} - \varepsilon + \frac{\partial}{\partial x_j}\left[(\nu + \nu_T/\sigma_k)\frac{\partial k}{\partial x_j}\right]$
Dissipatión rate	$\frac{\partial \varepsilon}{\partial t} + u_j\frac{\partial \varepsilon}{\partial x_j} = C_{\varepsilon 1}\frac{\varepsilon}{\kappa}\tau_{ij}\frac{\partial u_i}{\partial x_j} - C_{\varepsilon 2}\frac{\varepsilon^2}{k} + \frac{\partial}{\partial x_j}\left[(\nu + \nu_T/\sigma_\varepsilon)\frac{\partial \varepsilon}{\partial x_j}\right]$

Table 2
The k–ω model of turbulence

Kinematic eddy viscosity	$v_T = k/\omega$
Turbulence kinetic energy	$\frac{\partial k}{\partial t} + u_j \frac{\partial k}{\partial x_j} = \tau_{ij} \frac{\partial u_i}{\partial x_j} - \beta * k\omega + \frac{\partial}{\partial x_j}\left[(v + \sigma^* v_T)\frac{\partial k}{\partial x_j}\right]$
Specific dissipation rate	$\frac{\partial \omega}{\partial t} + u_j \frac{\partial \omega}{\partial x_j} = \alpha \frac{\omega}{\kappa} \tau_{ij} \frac{\partial u_i}{\partial x_j} - \beta\omega^2 + \frac{\partial}{\partial x_j}\left[(v + \sigma v_T)\frac{\partial \omega}{\partial x_j}\right]$
Closure coefficients and auxiliary relations	
$\alpha = \frac{13}{25}, \quad \beta = \beta_0 f_\beta, \quad \beta^* = \beta_0^* f_{\beta^*}, \quad \sigma = \frac{1}{2}, \quad \sigma^* = \frac{1}{2}$	
$\beta_0 = \frac{9}{125}, \quad f_\beta = \frac{1+70\chi_\omega}{1+80\chi_\omega}, \quad \chi_\omega \equiv \left\lvert \frac{\Omega_{ij}\Omega_{jk}S_{ki}}{(\beta_0^*\omega)^3} \right\rvert$	
$\beta_0^* = \frac{9}{100}, \quad f_{\beta^*} = \begin{cases} 1, & \chi_k \leqslant 0 \\ \frac{1+680\chi_k^2}{1+400\chi_k^2} & \chi_k > 0 \end{cases}, \quad \chi_k = \frac{1}{\omega^3}\frac{\partial k}{\partial xj}\frac{\partial \omega}{\partial xj}$	
$\varepsilon = \beta^*\omega k$ and $\ell = k^{1/2}/\omega$	

$$\frac{\partial C}{\partial t} + u\frac{\partial C}{\partial x} + v\frac{\partial C}{\partial y} + w\frac{\partial C}{\partial z} = D_{\text{eff}}\left(\frac{\partial^2 C}{\partial x^2} + \frac{\partial^2 C}{\partial y^2} + \frac{\partial^2 C}{\partial z^2}\right) \tag{7}$$

In this equation D_{eff} is the effective mass transfer diffusivity, which is equal to the summation of molecular and turbulent diffusivities:

$$D_{\text{eff}} = D_0 + \frac{\mu_t}{\rho Sc_t} \tag{8}$$

where D_0 is the molecular diffusivity of a tracer, μ_t is the turbulent viscosity. Since turbulent flow generally carries mass over an equivalent Prandtl mixing length the turbulent Schmidt number Sc_t was assumed equal to one. Mass transfer was simulated solving Eq. (7) based on the velocity fields calculated by the three models of turbulence k–ε, k–ω and RSM.

3.5. Boundary and initial conditions

3.5.1. k–ε model

To deal with flow modeling of near wall region the wall functions by Launder and Spalding are employed [18]. No-slipping conditions were applied as boundary conditions to all solid surfaces of the tundish. At the entry, above the blade, and at the outlets flat velocity profiles are assumed (see Fig. 4) and are calculated by

$$U_{\text{in}} = Q/A_{\text{nozzle}} \tag{9}$$

The inlet values for k and ε at the inlet were calculated with the following equations:

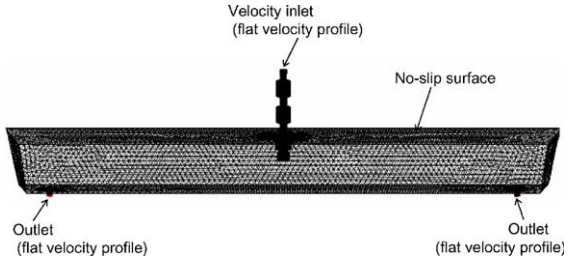

Fig. 4. Three-dimensional view of the unstructured mesh and boundary conditions used in the model.

$$k_{\text{in}} = 0.01U_{\text{in}}^2 \tag{10}$$

$$\varepsilon_{\text{in}} = 2k_{\text{in}}^{3/2}/D_{\text{nozzle}} \tag{11}$$

Gradients of the turbulent kinetic energy and its dissipation rate are zero at the symmetry planes and at the free bath surface. No swirling boundary conditions were imposed at the SLS entrance to avoid induced swirling motion. Then swirling would eventually appear as a consequence of the presence of the blade itself. The velocity of liquid at the entry of the LS or SLS, U_i, was 0.77 m/s.

3.5.2. k–ω model

Wall boundary conditions for the velocity field are treated in the same way as in the k–ε model including the near wall approach through empirical functions. The same can be said about the inlets and outlets of fluid in the tundish. Regarding the wall function for ω the following expression was applied [12];

$$\omega = \frac{k^{1/2}}{\beta_0^* \kappa y} \tag{12}$$

where β_0^* is an empirical constant which value is presented in Table 2, κ is the Von Kármán constant and y is the perpendicular distance from the wall surface. Surface roughness was not considered in this work; gradients of k and ω at the symmetric planes including the bath surface are zero. Boundary conditions at the inlet and the outlets of this tundish for k and ω are similar to the previous turbulence model.

3.5.3. The RSM model

At walls, explicit boundary conditions are applied using log-law expressions disregarding convection and diffusion in the transport equations for the stresses in Eq. (3). Reynolds stresses at the adjacent cells to a wall are computed from

$$\frac{\overline{u_\tau'^2}}{k} = 1.098, \quad \frac{\overline{u_j'^2}}{k} = 0.247, \quad \frac{\overline{u_\lambda'^2}}{k} = 0.655$$
$$-\frac{\overline{u_\tau' u_\eta'}}{k} = 0.255 \tag{13}$$

Boundary conditions for gradients k and ε at walls and the free bath surface and inlet conditions for these two scalars are similar to the two precedent molds.

3.5.4. Mass transfer

The velocity field calculated with any of the three turbulence models was then employed to solve Eq. (7) for the tracer concentration under unsteady state conditions. Here, it is implicitly assumed that the presence of the tracer does not affect the water density to any appreciable extent. The initial condition to solve Eq. (7) is stated as follows:

$$\text{at} \quad t = 0 \quad \text{and} \quad x_0, y_0, z_0 \quad C = \frac{M}{V_{\text{nozzle}}} \tag{14}$$

where M is the total mass of the tracer and V is the volume of the water column in the ladle shroud from the injection point to the shroud tip assuming a perfect mixing. x_0, y_0 and z_0 are the coordinates of the nozzle tip in the 3D domain. Since the injection time (3 seconds) is negligible compared with the total duration of an experiment it was assumed that the concentration expressed by Eq. (14) was attained instantaneously.

All simulations were performed for water with physical properties of viscosity of 0.001 Pa s and a density of 1000 kg/m^3. Calculating velocity fields of water allows a direct comparison with the experimental flow fields determined using the PIV technique. This approach will be useful to define which of the three turbulence models is capable to emulate more closely the actual experimental observations of water flow in the tundish model.

The Eqs. (1) to (7) have been solved by employing a finite volume technique. The discretized equations finally result in a set of linear algebraic equations by using the scheme SIMPLEC [19] as the pressure-velocity coupling. The linear set of equations is solved through the commercial CFD code Fluent by using its inbuilt algebraic multigrid solver. Computation convergence was obtained when the residuals of the output variables like velocities, pressure, Reynolds stresses reached values lower than 1×10^{-5}. The hybrid mesh employed to perform the computations consisted of 139 804 hybrid hexahedral and tetrahedral cells involving the physical domain. Trials using a larger number of cells did not improve the errors below 1%. All mathematical simulations were performed in two PC's at 3.1 GHz with RAM memories of 2 G-Bytes at the Laboratory of Mathematical Simulation of Materials Processing and Fluid Dynamics of IPN-ESIQIE. Fig. 4 shows the computational mesh employed in these simulations.

3.6. Trajectory of inclusions

Inclusion trajectories were calculated using a Lagrangian particle tracking approach [20], which solves a transport equation for each inclusion as it travels through the previously calculated flow field of water. The mean local-inclusion velocity components (v_{pj}) needed to obtain the particle path are calculated from the following balance, which includes the drag and buoyancy forces relative to water equation (20)

$$\frac{\mathrm{d}v_{p,i}}{\mathrm{d}t} = \frac{18\rho\nu}{\rho_p d_p^2}(1 + 0.15Re_p^{0-687})(u_i - v_{p,i}) \tag{15}$$

where v_{pj} is the particle velocity along a trajectory "j", ρ_p its density, d_p its diameter, ρ is density of liquid, μ is viscosity and u_i is the liquid velocity. Reynolds number is calculated through,

$$Re_p = \frac{d_p|u - v_p|}{\nu} \tag{16}$$

To simulate the chaotic effect of the turbulence eddies on the inclusion trajectories; a discrete random-walk model was applied [21]. In these simulations a fluctuant random-velocity vector of the fluid, (u_i'), is added to the calculated time-averaged vector ($\bar{u}_i$) in order to obtain the inclusion velocity (v_{pi}) at each time step as a particle travels through the fluid. Each random component of the fluid velocity is proportional to the local turbulent kinetic energy level, according to the following equation:

$$u_i' = \zeta_i \sqrt{\bar{u}_i'^2} = \zeta_i \sqrt{\frac{2k_p}{3}} \tag{17}$$

where ξ is a random number, normally distributed between -1 and 1, which changes at each integration step and k_p is the kinetic energy at node p. The scalar field of the turbulent kinetic energy used in Eq. (17) was calculated with the k–ε and RSM models for a tundish equipped with a LS and a SLS, respectively. Once the

fluid velocity field and the velocity of inclusions are known the integration of their trajectories were calculated through Eq. (18),

$$s = \int_0^t v_{p,j}\,\mathrm{d}t \tag{18}$$

Those inclusions that reach the top free surface of the bath and the tundish outlets have boundary conditions of trap and escape, respectively. In order isolate the effects of buoyancy forces on the particles trajectories boundary conditions including totally elastic impacts on the tundish walls and its bottom were applied.

4. Results and discussion

4.1. Mathematical simulations of fluid flow with different turbulence models

Simulations of fluid flow inside the SLS are shown in Fig. 5a–c using the k–ε, k–ω and RSM, respectively. The three turbulence models predict intensive swirling after the fluid leaves the blade; fluid rotation velocities reach high magnitudes especially at the position of the blade and in the first chamber. Rotation speeds decrease in the downward chambers. Apparently there are not appreciable differences among the flow fields predicted by these models. Nevertheless, predicted velocity profiles, using the three turbulence models, at the horizontal-plane of the SLS exit show some basic differences. The RSM predicts slightly higher peripheral velocities as is marked by number "1" in Fig. 6, than corresponding velocities calculated through the k–ε and k–ω models. These differences of velocity have a great influence on the fluid flow pattern developed inside the tundish as will be explained later. It is important to mention that neither the RSM nor the k–ω models predict correctly the flow in a tundish using the LS as the simple k–ε does. For example, Fig. 7a shows PIV measurements which must be compared with simulation results given in Fig. 7b and c for the k–ε and RSM models, respectively. Points marked with numbers "1", "2" and "3" in Fig. 7a have an acceptable correspondence with those predicted in Fig. 7b. The flow characteristics at those three points do not keep agreement with those present in Fig. 7c with the exception of point "3".

Fig. 8a–c show the steady-sate velocity fields at the symmetrical-longitudinal plane of the tundish calculated with the turbulence models k–ε, k–ω and RSM, respectively. It is observed that the flows are symmetrical particularly those predicted by the models k–ε and k–ω. Both models predict also similar fluid flow patterns with small differences in the locus lines of the free shear stress flows marked with numbers 1 and 2. These models also indicate the existence of recirculating flows at both sides of the entry jet promoted by the entrainment of the surrounding fluid. On the other hand, a small flow asymmetry is predicted by the RSM model (Fig. 8c), the recirculating flows at both sides of the entry jet at the tundish bottom are flatter. A stagnant zone is seen at zones marked with number "3". Fig. 9a–c show the distribution maps of kinetic energy for the right sides of Fig. 8a–c, respectively. Again, the first two models predict similar maps and magnitudes of this scalar; high levels of turbulence at the jet entry and at a small volume located in the outlet are observed. Moreover, the k–ε and k–ω models predict high turbulence at the outlet with a magnitude similar to that observed at the entry jet. Different to the other models the RSM predicts smaller turbulent kinetic energy values than the two previous models. Kinetic energy is considerably smaller throughout the fluid volume showing an effective decrease of flow turbulence. It is worthy to mention that these differences between the RSM, the k–ε & k–ω models are large in spite of the close similarity of fluid flows inside the SLS as is seen in Fig. 5a and b. The three turbulence

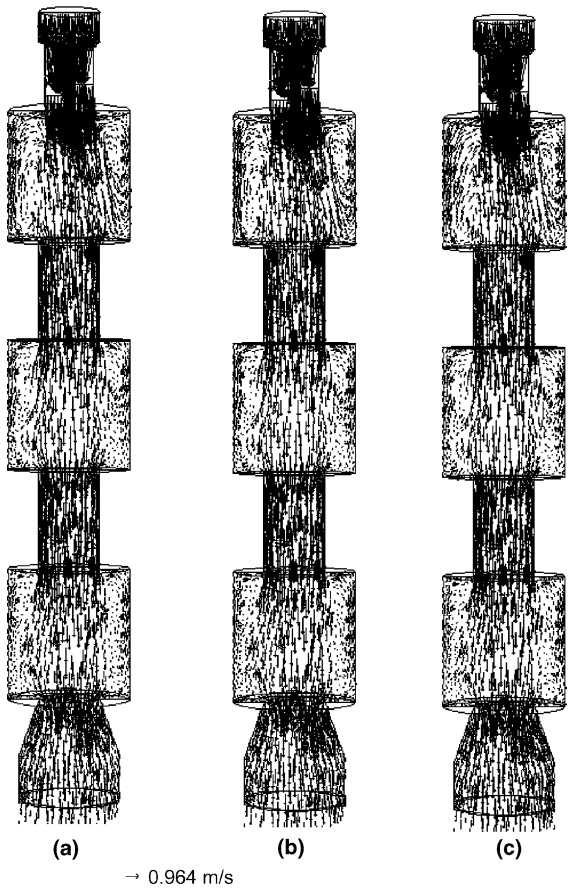

Fig. 5. Velocity fields at the transversal—symmetry plane of the swirling ladle shroud predicted mathematically using different models of turbulence: (a) k–ε model, (b) k–ω model and (c) RSM model.

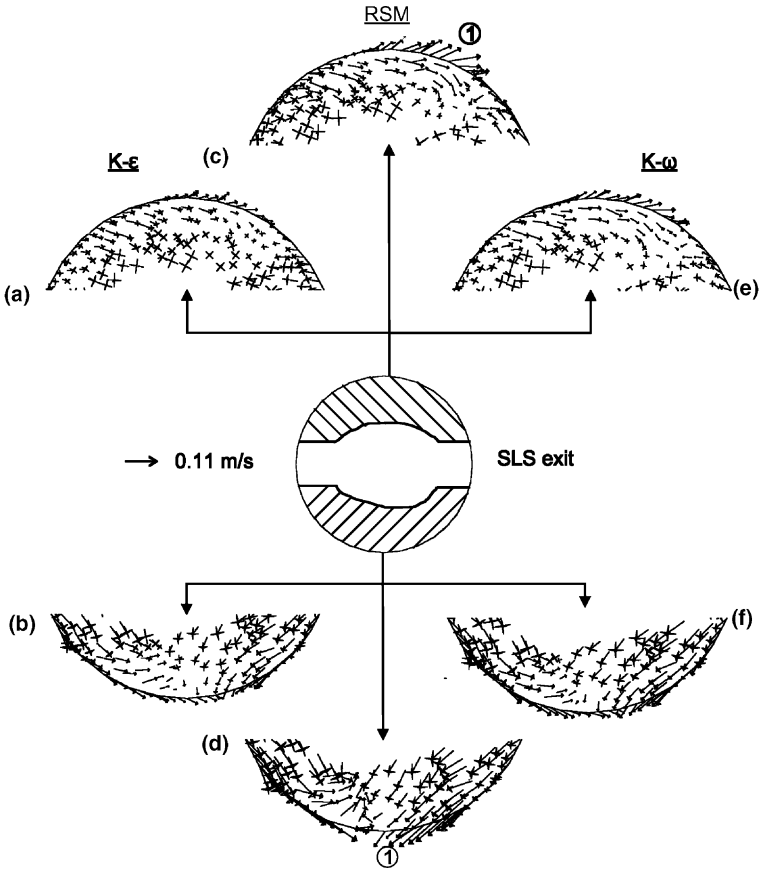

Fig. 6. Velocity fields at the horizontal plane of the SLS exit: (a) and (d) k–ε model, (b) and (e) RSM model, (c) and (f) k–ω model.

models predict growing gradients of the turbulent kinetic energy from the bath free surface and from the tundish bottom toward the central part following highly energy stratified flow structures.

Fig. 10a–c show the velocity fields at the symmetrical-transversal plane of this tundish as predicted by the k–ε, k–ω and RSM models, respectively. Again averaged non-symmetrical flows are well evident in this plane due to the swirling action exerted by the SLS on the fluid flow. However, it is also true that the two k–ε and k–ω models predict similar flow patterns; the first two models indicate the formation of recirculating flows formed by the entry jet, which entrains the surrounding liquid involving the full bath height, the RSM predicts clearly the swirling motions of the fluid. Thus the fluid moves with recirculations acting at horizontal and transversal planes. This flow pattern will be corroborated in Section 4.3.

4.2. Mass transfer simulations with different turbulence models

In order to validate the appropriated turbulence model for simulating fluid flow and mass transfer the experimental mass transfer data of the red dye tracer were compared directly with the mathematical predictions using the three models of turbulence. Fig. 11a shows a video-photo of tracer dispersion after 9 s of its injection in the SLS and Fig. 11b and c show the mathematical predictions using the models of turbulence k–ε and k–ω, respectively. As is seen both models predict convex shaped mixing fronts while the experimental profile in Fig. 11a indicates the formation of a "S" shaped mixing front. Additionally, both models predict the high concentrations of the tracer in a location, which is close to the tundish bottom. The concentration field predicted by the RSM model corresponding to Fig. 11a–c is shown in Fig. 11d and, as seen, this model predicts acceptably well the "S" shape of the mixing front observed in Fig. 11a. Moreover, the highest concentrations predicted by the RSM model are located at the points marked with numbers "1" and "2" in Fig. 11d which agree with the strongest colorations observed in Fig. 11a, for the same points, that indicates high concentrations of the tracer in the actual experiment. Zones of relatively low concentrations are clearly seen in Fig. 11a, marked with numbers "3" and "4", and this is also acceptably well predicted by the corresponding indication

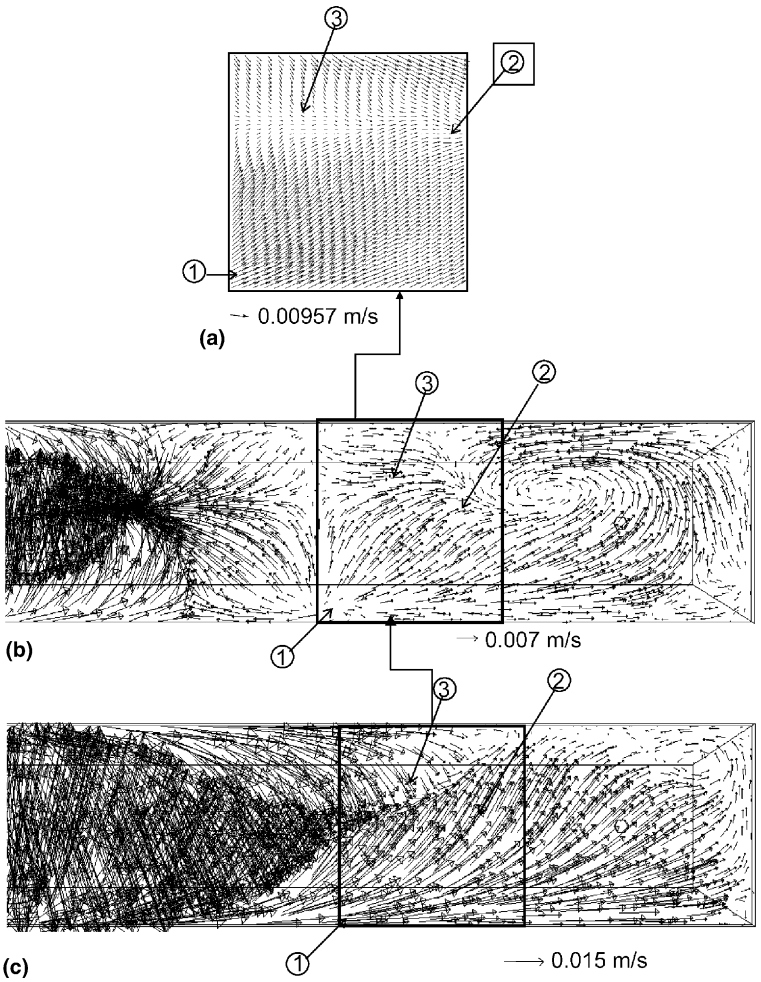

Fig. 7. Velocity fields at the horizontal plane close to the surface of the tundish determined by: (a) Particle image velocimetry (PIV), (b) k–ε model, and (c) RSM model in a tundish that is fed by a LS.

in Fig. 11d. The appropriateness of the RSM model to simulate swirling flows is provided by comparison between the experimental and predicted residence time distribution (RTD) curves of the tracer calculated with the three turbulence models as is shown in Fig. 12. As is seen, the three models approach the experimental curve but none of them agrees completely, rather the three models are close to each other. However, the RSM predicts very well the experimental minimum residence time of the tracer. The close agreement between the three models is probably related to similar turbulent diffusion contributions at the entry jet zone, which essentially governs the mixing kinetics of tracer.

4.3. Velocity fields simulated with RSM model compared with PIV measurements

Comparisons of experimental velocity fields and mathematical simulations using the RSM model of turbulence at the vertical-symmetric planes of the tundish are shown in Fig. 13a–d corresponding to the positions indicated in the central scheme. Fig. 13a shows the experimentally determined velocity field of a plane at position 1 and Fig. 13b shows the corresponding prediction by the RSM model. The existence of a recirculating "eye" marked with number "1" is observed in the lower bottom left corner of Fig. 13a and the predictions indicate the formation of this "eye" at approximately the same position as is seen in the point marked by number "1" in Fig. 13b. Experimental determinations indicate the existence of velocity vectors descending from the upper left corner as is seen in point marked with number "2" in Fig. 13a which has its equivalent in the point marked with number "2" in Fig. 13b. At point marked with number "3", Fig. 13a, velocity vectors are oriented toward the lower left corner and the same can be seen in the RSM model predictions in Fig. 13b, at point "3". Experimental results and mathematical predictions of

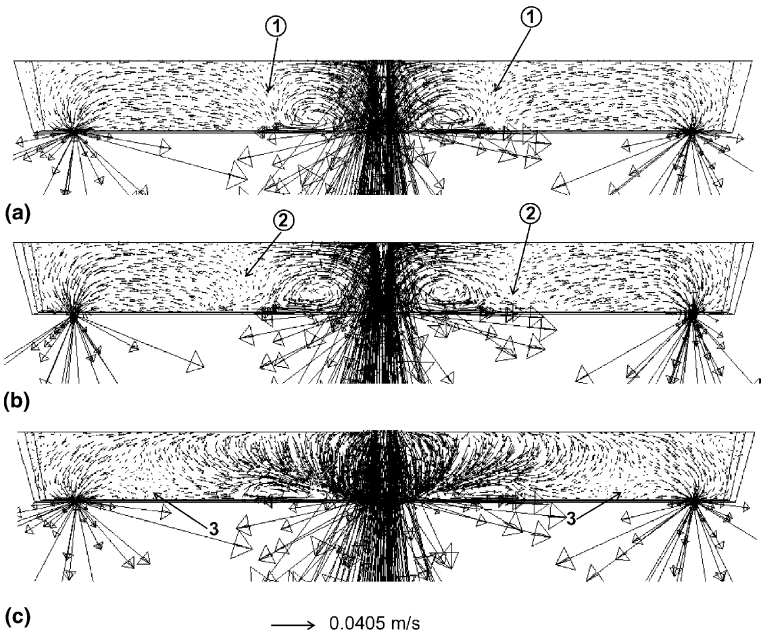

Fig. 8. Velocity fields at the vertical–symmetry plane predicted mathematically using different models of the turbulence and the swirling ladle shroud: (a) k–ε model, (b) k–ω model and (c) RSM model.

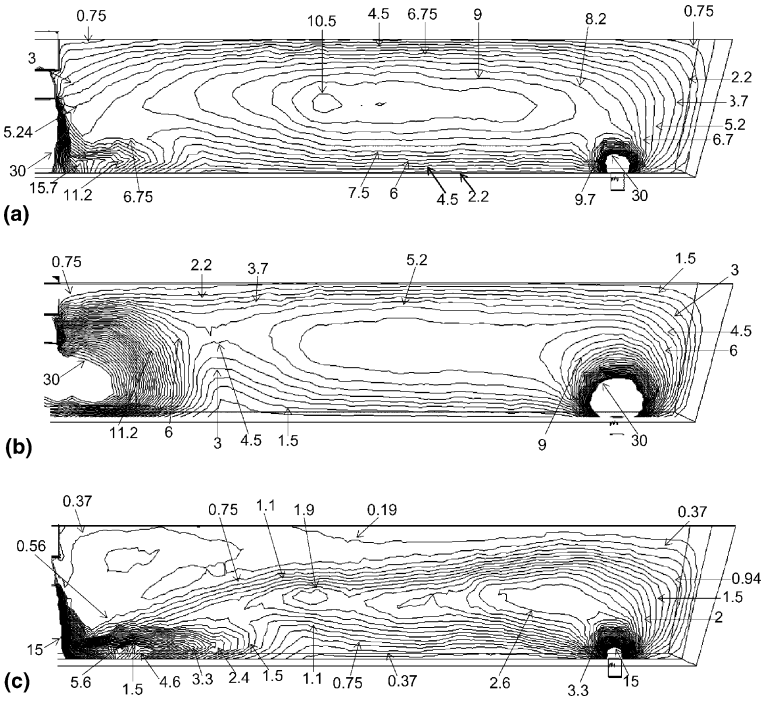

Fig. 9. Contours of the turbulence kinetic energy $\times 10^{-4}$ at the vertical—symmetric plane predicted mathematically using different models of turbulence and the swirling ladle shroud: (a) k–ε model, (b) k–ω model and (c) RSM model.

velocity fields in the outlet box (plane 2 in the central scheme) are shown in Fig. 13c and d, respectively. Then, by observing the agreement between points marked with numbers "1", "2", and "3", regarding the velocity field,

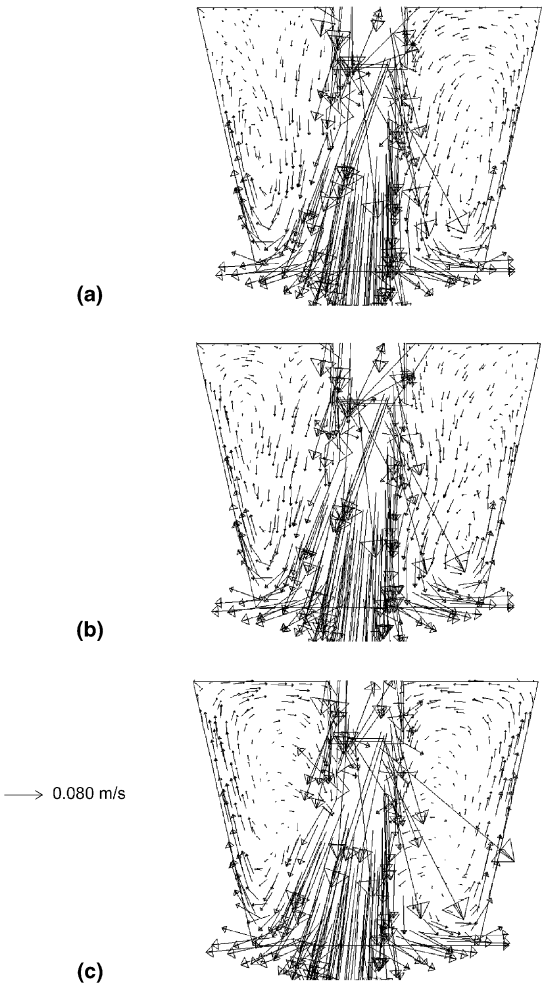

Fig. 10. Velocity fields at the transversal-symmetry plane predicted mathematically using different models of turbulence and the swirling ladle shroud: (a) k–ε model, (b) k–ω model and (c) RSM model.

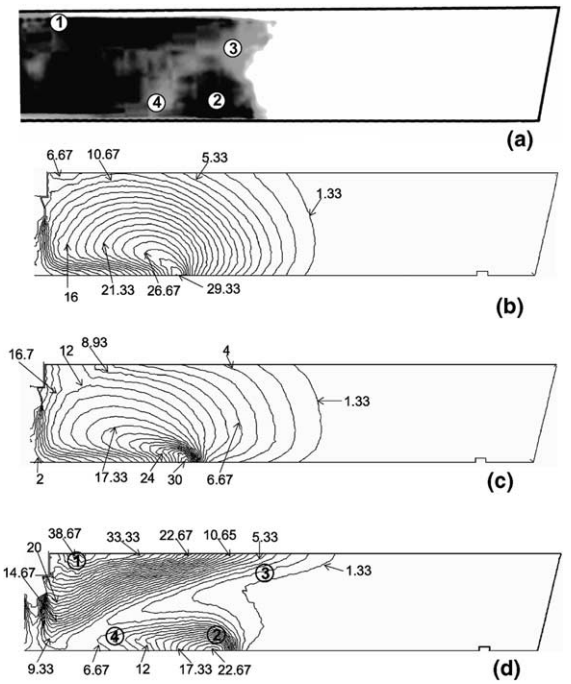

Fig. 11. A simulated concentration contours in mass% $\times 10^{-4}$, 9 s after injection of the tracer in the tundish using the swirling ladle shroud. (a) Video image of the tracer dispersion in the flow, (b) mathematical simulations of tracer, using the k–ε model, (c) tracer dispersion using the k–ω model and (d) tracer dispersion using the RSM model.

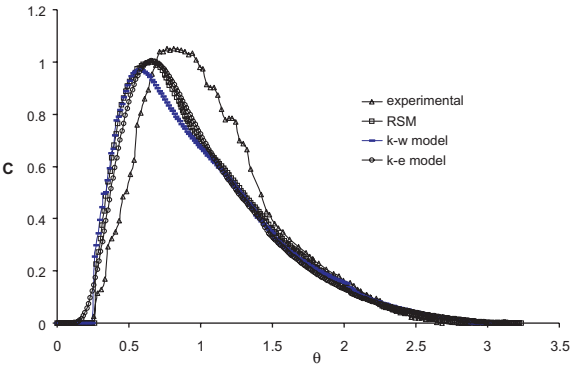

Fig. 12. Experimental and simulated residence time distribution curves, using the swirling ladle shroud.

in these two Figures we can affirm that indeed the RSM model of turbulence is able to predict acceptably well the experimental observations.

In the horizontal planes it was observed, through the PIV measurements, that the fluid flow is still more complex due to the horizontally swirling-rotating motion of the entry jet as is imposed by the SLS. Fig. 14a and b show the experimental and mathematically simulated velocity fields at a horizontal plane respectively located at half the liquid level in the tundish, as is indicated in the central scheme. Here the PIV planes are smaller than the complete computational plane and this view is to emphasize the correct position of the experimental plane. Point marked with number "1" in Fig. 14a (this view involves only about 2/3 of the tundish width) shows an "eye" of the recirculating flow promoted by the swirling entry jet which is also observed in the predicted results with number "1" in Fig. 14b (this view involves the complete tundish width) located slightly closer to the front wall of the tundish. Swirling flow in the

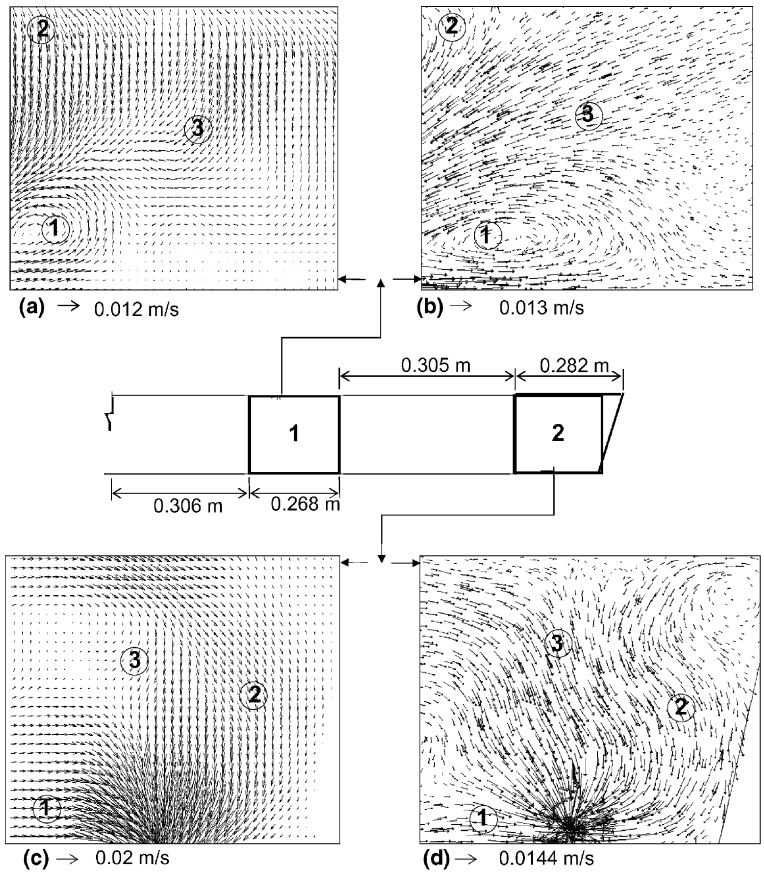

Fig. 13. Measured and mathematically predicted velocity fields using the RSM model at the vertical–symmetric planes: (a) PIV measurements at plane 1, (b) mathematical predictions at plane 1, (c) PIV measurement at plane 2 and (d) mathematical predictions at plane 2.

horizontal planes is detected in Fig. 10c as was described in Section 4.1. For example, fluid flow in points marked with number "2" in Fig. 14a and b agree also since both show that the fluid flows upstream as a part of a large recirculating flow. Fluid flow in points marked with number "3" in Fig. 14a and b agree clearly in the downstream orientation of the velocity vectors. Further comparisons between experimental determinations and mathematical simulations are observed in Fig. 14c and d respectively for a horizontal plane located as is indicated in the central scheme (plane 2). Points marked with number "1" in Fig. 14c and d show the same downstream orientation of the velocity vectors, besides, points marked with number "2" in both Figures show acceptably good agreement about the existence of a free shear flow between two streams of fluid meeting at that point. Points marked with number "3" show the same downstream flow oriented toward the half height of the end wall. In summary, the mathematical predictions are in good agreement with the experimental measurements corroborating that the RSM turbulence model is recommendable to simulate swirling flows in a tundish.

4.4. Fluid flow and mass transfer with the conventional ladle shroud (LS) and the swirling ladle shroud (SLS)

As demonstrated by Vargas-Zamora et al. [3] and as was discussed in Fig. 7a–c, the k–ε model is suitable to simulate non-swirling flows produced by a conventional LS; the computational results are presented in Fig. 15a which shows the velocity field expressed as velocity contours in the vertical-symmetric plane in a tundish. Fig. 15b shows the corresponding velocity contours in a tundish, which is fed by a SLS calculated through the RSM model. Comparing both Figures it can be seen that the velocity contours of the entry jet using the SLS are considerably smaller than those provided by the LS. Thereby the velocity magnitudes of the liquid entrained by the entry jet using the SLS are also smaller than those corresponding to the case with the LS. Control of the fluid

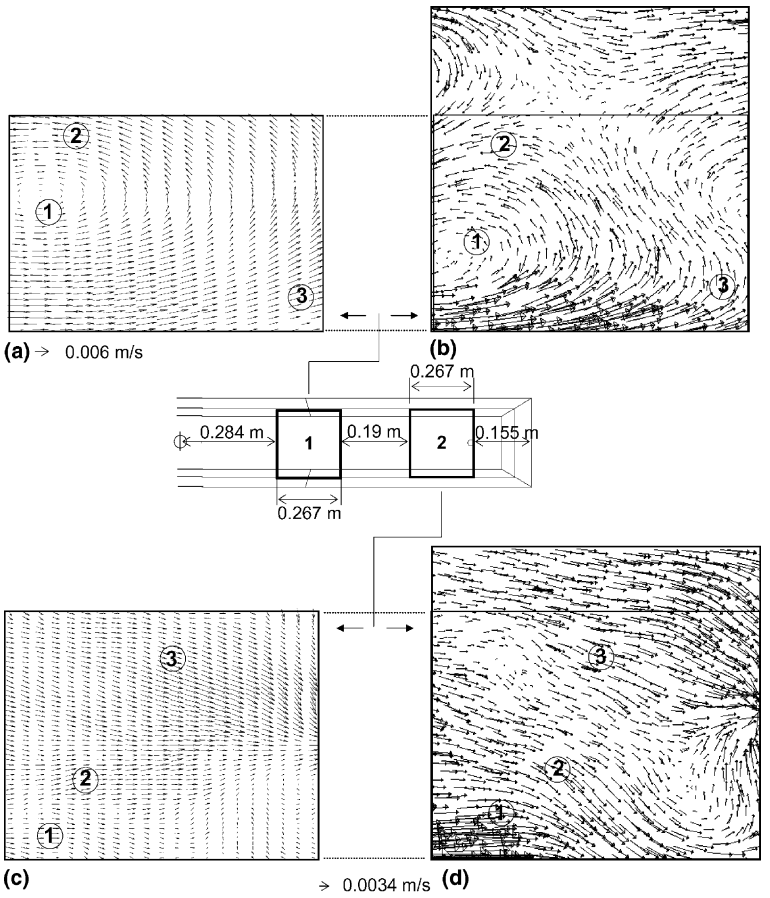

Fig. 14. Measured and mathematically predicted velocity fields using the RSM model at a symmetry-horizontal planes: (a) PIV measurements at plane 1; (b) mathematical predictions at plane 1; (c) PIV measurements at plane 2 and (d) mathematical predictions at plane 2.

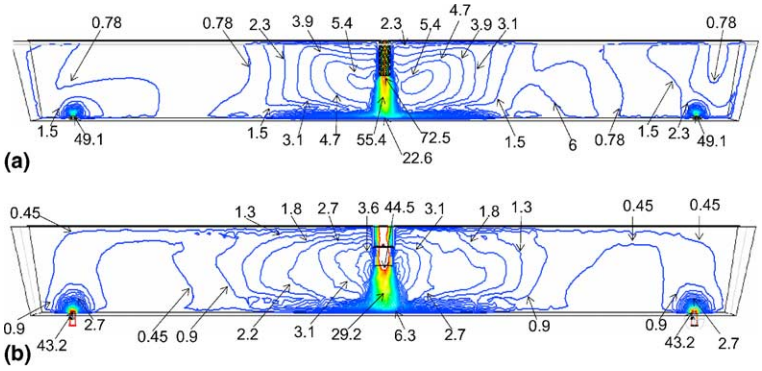

Fig. 15. Velocity contours $\times 10^{-2}$, at the vertical-symmetric plane predicted mathematically: (a) conventional ladle shroud and using the k–ε model, (b) swirling ladle shroud and using the RSM model.

flow turbulence can be seen directly through the distribution maps of the turbulent kinetic energy for flows with the LS and the SLS in Fig. 16a and b, respectively. The value of this scalar at the impact area of the entry jet, using the LS, is about 39×10^{-4} m^2/s^2 and the corresponding value using the SLS is about 15×10^{-4} m^2/s^2.

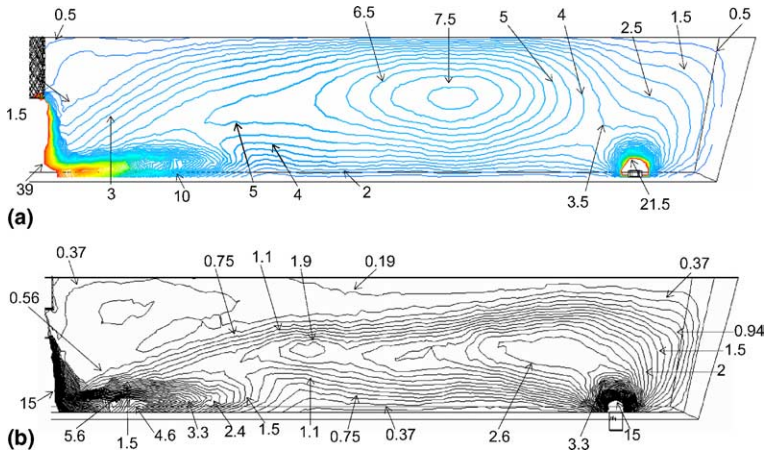

Fig. 16. Contours of the turbulent kinetic energy $\times 10^{-4}$ at the central plane predicted by mathematical simulation: (a) conventional ladle shroud and the k–ε model and (b) swirling ladle shroud and the RSM model.

Similar observations are applicable for the rest of both scalar maps. Then magnitudes of the turbulent kinetic energy of the fluid flow are considerably smaller using the SLS than using the LS probing the capacity of this device to control satisfactorily flow turbulence. Fig. 17 compares the experimental RTD curves of this tundish with the LS and the SLS and, as is seen, the SLS yields a longer minimum residence time and a higher concentration peak. All these characteristics indicate a higher volume fraction of fluid under plug flow with smaller dead volumes as is indicated in Table 3.

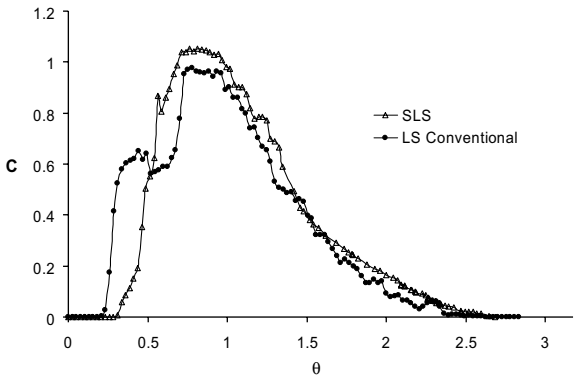

Fig. 17. Experimental residence time distribution curves, using the swirling ladle shroud and conventional ladle shroud.

4.5. Trajectory of inclusions

Using the same procedure of Vargas-Zamora et al. [3] through the solution of Eq. (15), the trajectory of inclusions with an assumed density of 500 kg/m^3 (which keeps a similar density ratio between inclusions of alumina and liquid steel) were calculated using the velocity fields predicted by the RSM model. Two size ranks of inclusions were considered; from 1 to 10 μm and from 10 to 50 μm. Results are presented in Fig. 18a and b for the tundish with LS for small and large inclusions, respectively. Fig. 18c and d show the same type of information for the tundish equipped with the SLS. Seven of ten small size inclusions leave the tundish with the LS and only three of ten small size inclusions leave the tundish employing the SLS. For large size inclusions one of ten and none of them leave the tundish using the LS and SLS, respectively. Further simulations increasing the number of inclusions in the field showed the same trend.

In the actual casting operation the use of a blade inside of ladle shroud is certainly not free of problems. One of them is its probable clogging by the sand in the outlet nozzle, which is used to avoid the direct contact of steel with the plates of the slide gate. Nevertheless, the present results indicate the feasibility of using swirling motions to improve fluid flow and flotation of inclusions. Further work must be focused on other methods to produce swirling of the steel entry into the tundish. This is an activity under current development at the author's laboratory.

Table 3
Estimation of dead, plug and mixed volume in the tundish as a function of ladle shrouds

Ladle shrouds	Dead volume (%)	Plug volume (%)	Mixed volume (%)	Average residence time
Conventional ladle shroud	13.36	25.81	60.83	115
Swirling ladle shroud	3.22	45.83	50.95	117

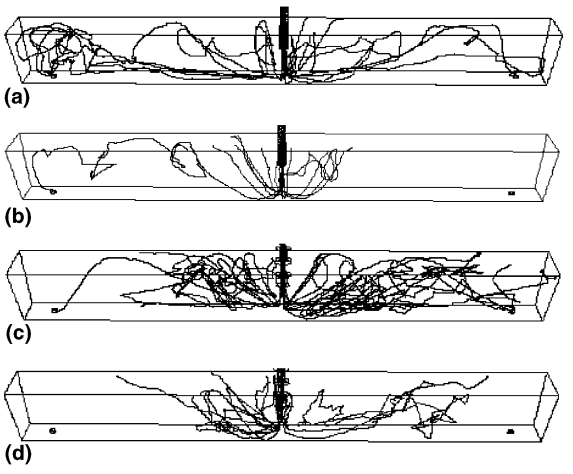

Fig. 18. Trajectories of inclusions in the water flow: (a) and (b) using the conventional ladle shroud and particle sizes from 1 to 10 μm and 10 to 50 μm respectively; (c) and (d) using the swirling ladle shroud and particle sizes from 1 to 10 μm and 10 to 5 μm respectively.

5. Conclusions

Experimental and mathematical simulations of liquid steel, using a water model, have been presented using two types of ladle shroud; a conventional piped design (LS) and a swirling ladle shroud (SLS) that dissipates the turbulent energy by a rotational motion of the entry jet in the tundish. The conclusions derived from this study are as follows:

1. Tracer dispersion can be accurately predicted by the RSM model while the k–ε and the k–ω models show poor prediction.
2. The Reynolds stress model proved to be efficient enough to simulate acceptably well the velocity fields determined experimentally by PIV measurements.
3. The three turbulence models predict close results among themselves for predicting RTD curves, although the RSM observes the best agreement with the experimental minimum residence time.
4. The SLS controls turbulence by dissipating the turbulence energy through rotational motions in horizontal and vertical planes inside the tundish volume.
5. The SLS improves flow parameters and shows a higher capability to float inclusions than any conventional LS.

Acknowledgement

The authors are very indebted to the institutions CoNaCyT, SNI and COFAA for their invaluable support to the Mathematical Simulation of Materials Processing and Fluid Dynamics Group of the National Polytechnic Institute.

Appendix A. Calculation of flow parameters

Mass transfer results were plotted using dimensionless concentration and time variables defined by (see nomenclature of symbols).

$$C = \frac{C_i}{(M/Q)} \tag{A.1}$$

$$\theta = \frac{t}{\bar{t}}$$

where the mean residence time is given by,

$$\bar{t} = \frac{\Sigma C_i t_i}{\Sigma C_i} \tag{A.2}$$

This plot is shown in Figs. 10 and 15 for the experimental results obtained through the recordings of the spectrophotometer and for the mathematical simulations obtained form the computer files. This comparison demonstrates the usefulness of mathematical simulations to describe mass transfer phenomena under isothermal conditions. One point to be noticed is the long minimum residence time of the tracer inside the vessel whose magnitude is directly related with the volume fraction of fluid that obeys the plug flow. Using the statistical methods, that are well known in the chemical engineering field [22,23], the volume fractions of fluid under plug flow, back mixing flow and dead non-interactive volume were calculated from the residence time distribution (RTD) curve using the following relationships:

$$\frac{V_p}{V} = \theta_{min} \tag{A.3}$$

where V_p is the fluid volume that follows a plug flow pattern, V is the total fluid volume in the vessel and θ_{min} is the minimum dimensionless residence time. All fluid volume remaining inside the vessel for dimensionless times greater than 2.0 can be regarded as dead volume. Dead volume is calculated through;

$$\frac{V_d}{V} = 1 - \theta\frac{Q}{V} \tag{A.4}$$

and the mixed fraction will be,

$$\frac{V}{V_m} = 1 - \left(\frac{V_p}{V} + \frac{V_d}{V}\right) \tag{A.5}$$

List of symbols of appendix

C	concentration of the tracer
Q	flow rate
θ	dimensionless time
$\bar{t}$	average time
V	total fluid volume

V_p plug volume
V_d dead volume
V_m mixed volume

References

[1] L.J. Heaslip, A. Mc Lean, I.D. Sommerville, Continuous Casting vol. 1, Iron and Steel Society, Warrendale, PA, 1983, pp. 99–112.

[2] S. López-Ramírez, J. de J. Barreto, J. Palafox-Ramos, R.D. Morales, D. Zacharias, Modeling study of the influence of turbulence inhibitors on molten steel flow, tracer dispersion and inclusions trajectories in tundishes, Metall. Trans. B 32B (2001) 615–627.

[3] A. Vargas-Zamora, R.D. Morales, M. Díaz-Cruz, J. Palafox-Ramos, L. García-Demedices, Heat and mass transfer of a convective-stratified flow in a trough type tundish, Int. J. Heat Mass Transfer 46 (2003) 3029–3039.

[4] S. López-Ramírez, R.D. Morales, A. Serrano, Numerical simulation of the effects of buoyancy forces and flow control devices on fluid flow and heat transfer of liquid steel in a tundish, Numer. Heat Transfer 37 (2000) 63–74.

[5] R.D. Morales, S. López-Ramírez, J. Palafox-Ramos, D. Zacharias, Mathematical simulation of the effects of flow control devices and buoyancy forces on molten steel flow and evolution of output temperatures, Ironmaking Steelmaking 28 (2001) 33–43.

[6] R.D. Morales, J. De J. Barreto, S. López-Ramírez, J. Palafox-Ramos, M. Díaz-Cruz, Mathematical simulation of the influence of buoyancy forces on molten steel flow in a continuous casting tundish, Model. Simul. Mater. Sci. Eng. 8 (2000) 781–801.

[7] A. Ramos-Banderas, R.D. Morales, L. García-Demedices, M. Díaz-Cruz, Mathematical simulation and modeling of steel flow with gas bubbling in trough type tundishes, ISIJ Int. 43 (2003) 653–662.

[8] W.P. Jones, B.E. Launder, The prediction of laminarization with a two-equation model of turbulence, Int. J. Heat Mass Transfer 15 (1972) 301–314.

[9] F.C. Lockwood, C.A. Romo-Millanes, Mathematical modeling of fuel-NO emissions from PF burners, J. Int. Energy 65 (1992) 144–152.

[10] R.D. Morales, S. López-Ramírez, J. Palafox-Ramos, D. Zacharias, Numerical and modeling analysis of fluid flow and heat transfer of liquid steel in a tundish with different flow control devices, ISIJ Int. 39 (1999) 455–462.

[11] B.E. Launder, N. Shina, Second-moment closure for the near wall sublayer: Development and application, AIAA J. 27 (1989) 1319–1325.

[12] D.C. Wilcox, Turbulence Modeling for CFD, second ed., LaCañada Industries, 2000, 123–125.

[13] B.E. Launder, Second-moment closure: Present .... and future? Int. J. Heat Fluid Flow 10 (1989) 282–300.

[14] B.J. Daly, F.H. Harly, Transport equations in turbulence, Phys. Fluids 13 (1970) 2634–2649.

[15] M.M. Gibson, B.E. Launder, Ground effects on pressure fluctuations in the atmospheric boundary layer, J. Fluid Mech. 86 (1978) 491–511.

[16] B.E. Launder, Second moment closure and its use in modeling turbulent industrial flows, Int. J. Numer. Methods Fluids 9 (1989) 963–985.

[17] S. Sarkar, L. Balakrishnan, Application of Reynolds stress turbulence model to compressible shear layer. ICASE Report 90-18 NASA CR 182002 (1990).

[18] B.E. Launder, D.B. Spalding, The numerical computation of turbulent flows, Comput. Methods Appl. Mech. Eng. 3 (1974) 269–289.

[19] T.J. Chung, Computational Fluid Mechanics, Cambridge University Press, 2002, 106–118.

[20] C. Crowe, M. Sommerfeld, Y. Tsuji, Multiphase Flows with Droplets and Particles, CRC Press, 2000, 57–106.

[21] D.I. Graham, P.W. James, Turbulent dispersion of particles using eddy interaction models, Int. J. Multiphase Flow 15 (1996) 157–165.

[22] O. Levenspiel, Chemical Reaction Engineering, Wiles & Sons, New York, Toronto, 1999.

[23] H.S. Fogler, Elements of Chemical Reaction Engineering, Prentice Hall, London, 1992.